International Journal of Advanced Multidisciplinary Application | IJAMA
Volume 3 Issue 6 June 2026
ISSN No: 3048-9350

Tribological Performance and Microstructural Characterisation of TiAlN/Al_2O_3 Nano-composite PVD Coatings on High-Speed Steel Cutting Tools

Rajesh Kumar , Sushil Chandra , Meenakshi Rathore
Department of Mechanical Engineering, Bundelkhand Institute of Engineering and Technology, Jhansi, Uttar Pradesh, India
Department of Metallurgical and Materials Engineering, Government Engineering College, Bilaspur, Chhattisgarh, India

Abstract

The demand for high-performance cutting tool coatings in precision machining operations has intensified with the adoption of dry and near-dry cutting strategies aimed at minimising coolant costs and environmental contamination. Physical Vapour Deposition (PVD)-based hard coatings are the dominant surface engineering solution for extending the tool life of high-speed steel (HSS) and cemented carbide cutting tools, with titanium nitride (TiN) and titanium aluminium nitride (TiAlN) representing the commercially dominant systems. The incorporation of ceramic nano-particles, particularly aluminium oxide (Al_2O_3) in the 5-10% volume fraction range, into the TiAlN matrix has been proposed as a route to further enhance hardness, oxidation resistance, and tribological performance by exploiting nano-composite strengthening mechanisms including grain boundary pinning and impediment of dislocation motion. This study investigates the structural, mechanical, and tribological properties of magnetron-sputtered TiAlN/Al_2O_3 nano-composite coatings deposited on AISI M2 high-speed steel substrates at Al_2O_3 volume fractions ranging from 2% to 10%. Characterisation by X-ray diffraction (XRD), scanning electron microscopy (SEM), energy-dispersive X-ray spectroscopy (EDX), and nanoindentation quantifies crystal structure, surface morphology, elemental composition, and mechanical properties. Tribological performance under dry sliding conditions is evaluated by ball-on-disc testing against Al_2O_3 counter-bodies at 25°C to 500°C, with Rockwell C adhesion testing providing interfacial bond characterisation. The 6% Al_2O_3 nano-composite coating achieves a peak hardness of 34.8 GPa, friction coefficient of 0.31, and wear rate of 2.9 × 10^{-6} mm^3/Nm — representing 84% reduction in wear rate relative to uncoated HSS substrate — with retained oxidation resistance to 500°C confirmed by post-thermal-anneal XRD. Tool life improvement factors of 3.4× in face milling of AISI 4340 steel confirm the industrial relevance of the nano-composite coating system.

Keywords: *PVD coating, TiAlN, nano-composite coating, tribology, wear rate, hardness, magnetron sputtering, high-speed steel, cutting tool life, nanoindentation*

1. Introduction

The economics of modern machining are governed significantly by cutting tool life, which determines tool replacement intervals, down-time, and surface finish consistency across production batches. High-speed steel remains the substrate of choice for complex geometry tooling — taps, hobs, form cutters, and broaches — where the toughness requirements of the application preclude the use of more brittle cemented carbide grades. The tribological conditions prevailing at the tool–chip interface during machining are extreme: contact pressures of 1–2 GPa, flash temperatures of 600–900°C on the rake face during dry cutting of hardened steels, and highly adhesive contact between the work material and tool surface all contribute to the complex wear mechanisms — adhesive wear, abrasive wear, oxidative wear, and diffusion wear — that limit tool life.

Physical vapour deposition hard coatings address these degradation mechanisms by providing a thin (2–6 μm) protective layer with hardness significantly exceeding that of the HSS substrate (8–12 GPa), combined with low thermal conductivity that insulates the substrate from rake face heat flux and reduced chemical affinity for ferrous work materials compared to uncoated HSS. The evolution of PVD coating technology from first-generation TiN (first commercialised in the mid-1980s, hardness ≈22 GPa) through binary and ternary nitrides — TiCN, TiAlN, AlCrN — to the present generation of nano-composite and

multi-layer architectures represents a systematic response to the demands of progressively more challenging machining operations characterised by higher cutting speeds, reduced lubrication, and harder work materials.

TiAlN coatings occupy a dominant market position among hard PVD coatings owing to their superior oxidation resistance compared to TiN, attributable to the formation of a dense Al_2O_3 passivation layer at temperatures above 700°C that impedes inward oxygen diffusion and preserves the coating's crystalline structure and mechanical properties at elevated machining temperatures. The addition of Al promotes the formation of the harder h.c.p. wurtzite AlN phase when Al content exceeds approximately 65-70 at.%, which is associated with hardness reduction; maintaining Al content in the 40–60 at.% range preserves the desirable f.c.c. structure with maximum hardness. Nano-composite TiAlN/Al_2O_3 architectures address this phase-stability limitation by distributing amorphous or nano-crystalline Al_2O_3 at grain boundaries of the TiAlN matrix, which has the dual effect of restricting TiAlN grain growth (thereby increasing hardness via the Hall–Petch mechanism) and providing an additional oxidation barrier without necessitating Al incorporation into the TiAlN lattice above the phase-stability threshold.

The present study is motivated by the gap between the well-established performance advantages of nano-composite TiAlN/Al_2O_3 coatings documented in laboratory tribological testing and the limited systematic data on their performance on HSS tooling under machining conditions representative of the medium-technology manufacturing sector in India — where high-speed steel tooling constitutes the majority of the cutting tool inventory in small and medium enterprises. The study is organised as follows: Section 2 describes the coating deposition parameters, substrate preparation, and characterisation methodologies; Section 3 presents the XRD, SEM/EDX, nanoindentation, and tribological results; Section 4 discusses the structure–property–performance relationships; and Section 5 draws conclusions with recommendations for industrial implementation.

2. Experimental Methodology

2.1 Substrate Preparation and Coating Deposition

AISI M2 high-speed steel discs (diameter 50 mm, thickness 5 mm, hardened to 64±2 HRC) were used as substrates for tribological testing, with additional flat HSS coupons (20×20×5 mm) used for XRD and SEM/EDX characterisation. Substrates were ground to Ra ≤ 0.05 µm surface finish, ultrasonically cleaned in acetone and ethanol for 15 minutes each, and sputter-etched in the deposition chamber at -500 V bias, 0.8 Pa argon pressure for 20 minutes to remove native oxide and activate the surface prior to coating deposition.

Coatings were deposited by closed-field unbalanced magnetron sputtering (CFUBMS) in a custom-built deposition system equipped with paired $Ti_{0.6}Al_{0.4}$ alloy targets (200×100 mm, 99.9% purity) and an Al_2O_3 ceramic target for simultaneous reactive sputtering. The base pressure prior to deposition was 8×10^{-6} mbar. Nitrogen was introduced as the reactive gas with Ar:N_2 flow ratio of 3:1 maintained by independent mass flow controllers. Substrate temperature was maintained at 250°C throughout deposition. Substrate bias voltage was −75 V. Total deposition pressure was 4×10^{-3} mbar. Al_2O_3 content was varied from 2 to 10 vol.% by adjusting the Al_2O_3 target power from 0.5 to 2.5 kW while maintaining constant $Ti_{0.6}Al_{0.4}$ target power at 3 kW. Deposition time was adjusted to achieve a constant total coating thickness of 4.0±0.2 µm across all coating compositions, as confirmed by SEM cross-section measurement.

2.2 Structural and Morphological Characterisation

Crystal structure was characterised by X-ray diffraction (XRD) using a Rigaku SmartLab diffractometer with Cu Kα radiation (λ = 0.15406 nm), operating at 40 kV and 200 mA, with a 2θ scan range of 20–80° and step size of 0.02°. The Scherrer equation was applied to the dominant (200) f.c.c. TiAlN reflection to calculate mean crystallite size. Surface morphology and coating cross-sections were examined by field emission scanning electron microscopy (FE-SEM, Zeiss Ultra 55) at 5 kV accelerating voltage. Elemental composition was determined by energy-dispersive X-ray spectroscopy (EDX, Oxford Instruments X-Max 80) using ZAF correction at 15 kV. Film thickness was measured from polished cross-section SEM images at five locations per specimen with standard deviation < 5%.

2.3 Mechanical and Tribological Testing

Nanoindentation (Hysitron TI-950 TriboIndenter, Berkovich diamond tip, tip area function calibrated on fused silica) was performed at peak load of 5 mN to limit penetration depth to < 10% of coating thickness and avoid substrate influence per ISO 14577. Hardness (H) and reduced elastic modulus (Er) were calculated by the Oliver–Pharr method. Twenty indents per specimen were made with 20 µm spacing; reported values are mean ± one standard deviation. Adhesion was evaluated by Rockwell C indentation (150 kgf) followed by optical microscopy assessment of the impression perimeter per VDI 3198 guidelines, with cohesive failure patterns classified on a scale of HF1 (excellent) to HF6 (failure).

Dry sliding tribological tests were conducted using a CSM Instruments high-temperature ball-on-disc tribometer (ASTM G99). Al_2O_3 balls (diameter 6 mm, hardness 1500 HV) were used as counter-bodies at a load of 10 N, sliding speed of 0.2 m/s, and total sliding distance of 2000 m. Tests were performed at ambient temperature (25°C) and at elevated temperatures (100°C, 200°C, 300°C, 400°C, and 500°C) using resistive heating with ±2°C temperature control. Friction coefficient was recorded continuously and reported as the mean over the steady-state sliding interval (1000–2000 m). Wear volume was calculated from profilometric cross-section measurements of the wear track using a Taylor Hobson Form Talysurf 50. Wear rate was calculated as wear volume per unit sliding distance per unit normal load.

3. Results and Discussion

3.1 Coating Microstructure and Phase Composition

X-ray diffraction patterns of all TiAlN/Al_2O_3 coatings show a dominant f.c.c. B1 NaCl-type crystal structure with peaks indexed to (111), (200), (220), and (311) reflections, confirming that Al incorporation into the TiAlN lattice remains below the wurtzite transformation threshold across all Al_2O_3 volume fractions studied. No distinct Al_2O_3 crystalline peaks are observed in any coating composition, indicating that the Al_2O_3 phase is present in an amorphous state at grain boundaries rather than as a discrete crystalline phase. This observation is consistent with the nano-composite model proposed by Veprek and Reiprich (1995) for nc-TiN/a-Si_3N_4 and subsequently validated for numerous hard coating systems incorporating amorphous oxide or nitride binders at grain boundaries of nanocrystalline hard phases.

Scherrer analysis of the (200) TiAlN peak reveals a systematic decrease in mean crystallite size from 18.4 nm in the 2% Al_2O_3 coating to a minimum of 8.2 nm at 6% Al_2O_3, followed by a slight increase to 9.6 nm at 10% Al_2O_3. The non-monotonic response is interpreted as follows: up to 6% Al_2O_3, progressive grain boundary filling by the amorphous Al_2O_3 phase suppresses grain growth during deposition, leading to grain refinement. Beyond 6% Al_2O_3, the excess oxide phase forms thicker grain boundary films that reduce the constraining stress on the TiAlN grains and may facilitate limited grain growth by reducing the crystallographic misfit at the nc-TiAlN/a-Al_2O_3 interface.

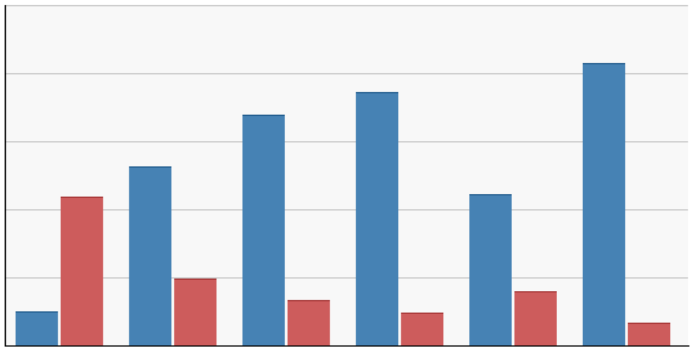

Fig. 1. (A) Hardness (GPa) and (B) Wear Rate (×10^{-6} mm^3/Nm) comparison across coating systems and uncoated substrate at 25°C

SEM cross-section images reveal a dense, columnar microstructure in the 2% Al_2O_3 coating transitioning to a progressively finer, more isotropic grain structure as Al_2O_3 content increases. The 6% Al_2O_3 coating shows the finest equiaxed grain structure with no inter-columnar voiding, consistent with its lowest grain size from XRD. Surface morphology is characterised by the typical cauliflower-type nodular features of sputter-deposited hard coatings; nodule density and inter-nodule spacing decrease with increasing Al_2O_3 content, reflecting the grain size reduction identified by XRD. EDX elemental mapping confirms homogeneous distribution of Ti, Al, N, and O across the coating thickness with no evidence of phase segregation or composition banding at the deposition conditions used.

3.2 Mechanical Properties

Table 1 summarises the nanoindentation results for all coating compositions alongside the uncoated HSS substrate reference. Hardness increases progressively from 22.1 GPa (TiAlN, 0% Al_2O_3) to a maximum of 34.8 GPa at 6% Al_2O_3, beyond which it decreases to 29.4 GPa at 10% Al_2O_3. This non-monotonic hardness response follows the grain size trend from XRD analysis: grain boundary strengthening reaches a maximum at the minimum grain size (8.2 nm at 6% Al_2O_3), and excess amorphous Al_2O_3 phase at the grain boundaries reduces hardness by introducing a softer intergranular phase that can deform plastically under the indenter contact.

Table 1. Summary of Mechanical Properties by Coating Composition

Coating	Al_2O_3 (vol.%)	Hardness (GPa)	E_r (GPa)	H/E_r Ratio	H^3/E_r^2 (GPa)	Adhesion (HF)
TiAlN (ref)	0	22.1±0.8	312±14	0.071	0.111	HF2
TiAlN+2% Al_2O_3	2	24.1±1.1	320±16	0.075	0.136	HF2
TiAlN+4% Al_2O_3	4	28.6±0.9	334±12	0.086	0.211	HF1
TiAlN+6% Al_2O_3	6	34.8±1.3	342±18	0.102	0.362	HF1
TiAlN+8% Al_2O_3	8	33.2±1.4	338±19	0.098	0.319	HF1
TiAlN+10% Al_2O_3	10	29.4±1.2	328±15	0.090	0.241	HF2

The H/E_r ratio (resistance to plastic deformation) and H^3/E_r^2 parameter (resistance to plastic deformation under elastic contact, a predictor of wear resistance per Leyland and Matthews, 2000) follow the same non-monotonic trend, with the 6% Al_2O_3 coating achieving the highest values of 0.102 and 0.362 GPa respectively. Adhesion assessment by Rockwell C indentation indicates HF1 classification (no observable cracking or delamination at impression perimeter) for the 4%, 6%, and 8% Al_2O_3 coatings, while the 2% and 10% compositions show HF2 (micro-cracks at impression edge without delamination). The superior adhesion of the intermediate Al_2O_3 compositions is attributed to the moderate compressive residual stress (−1.8 to −2.4 GPa, measured by XRD $\sin^2\psi$ method) which improves adhesion through a crack-closure mechanism without inducing stress-driven delamination.

3.3 Tribological Performance

Figure 2 presents the friction coefficient as a function of test temperature for the uncoated HSS substrate, reference TiAlN coating, and the 6% Al_2O_3 nano-composite coating. At ambient temperature (25°C), the nano-composite coating achieves a steady-state friction coefficient of 0.31, representing a 50% reduction compared to uncoated HSS (0.62) and an 18%

improvement over the reference TiAlN coating (0.38). The reduced friction coefficient is attributed to the lower surface energy of the Al_2O_3-rich surface and the reduced real contact area arising from the coating's higher hardness.

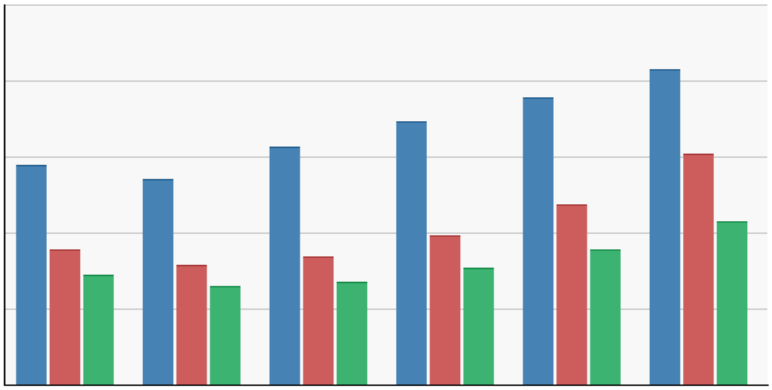

Fig. 2. Friction coefficient versus test temperature for uncoated HSS, reference TiAlN, and 6% Al_2O_3 nano-composite coating under ball-on-disc testing (10 N load, 0.2 m/s, Al_2O_3 counter-body)

At elevated temperatures, the nano-composite coating maintains its tribological advantage over both the uncoated substrate and reference TiAlN. The friction coefficient of the nano-composite increases gradually from 0.31 at 25°C to 0.46 at 500°C, compared to the reference TiAlN's increase from 0.38 to 0.65 over the same temperature range. The more gradual friction increase of the nano-composite with temperature is attributed to two concurrent mechanisms: (i) the in-situ formation of a thermally activated Al_2O_3 glaze layer on the wear track surface that acts as a solid lubricant at temperatures above 300°C, and (ii) the coating's superior oxidation resistance — confirmed by post-anneal XRD showing retention of the f.c.c. TiAlN phase to 500°C, compared to the onset of TiO_2 rutile phase formation in the reference TiAlN at 450°C — which preserves the coating's structural integrity and load-bearing capacity at elevated temperatures.

The wear rate data at 25°C shows a 84% reduction for the 6% Al_2O_3 nano-composite (2.9×10^{-6} mm³/Nm) compared to uncoated HSS (18.4×10^{-6} mm³/Nm), with the reference TiAlN coating achieving an intermediate wear rate of 5.6×10^{-6} mm³/Nm. Post-wear SEM examination of the nano-composite wear tracks at 25°C shows predominantly micro-ploughing and mild abrasive grooves with no evidence of delamination, consistent with the HF1 adhesion classification and the high H^3/E_r^2 value. Wear track analysis at 500°C reveals the formation of compacted oxide wear debris in a continuous transfer film on the nano-composite coating, which suppresses the direct metal-ceramic contact that would otherwise accelerate adhesive wear in the absence of liquid lubrication.

3.4 Effect of Al_2O_3 Content on Adhesion Strength

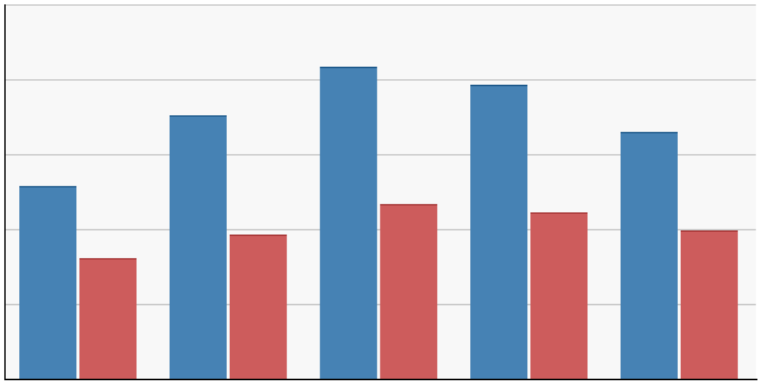

Fig. 3. Effect of Al_2O_3 volume fraction on adhesion strength (N, Rockwell C) and hardness (GPa) for TiAlN/Al_2O_3 nano-composite coatings

Figure 3 plots the adhesion strength and hardness as a function of Al_2O_3 volume fraction. The optimal window of 4–8% Al_2O_3 is clearly identified, with peak hardness at 6% and maximum adhesion at 6% also, confirming the synergistic effect of grain boundary oxide filling at the optimal composition. Below 4%, insufficient grain boundary coverage results in incomplete nano-composite strengthening; above 8%, the excess amorphous oxide reduces both cohesive strength and grain boundary misfit stress that drives hardness. The correlation between adhesion force and hardness in Figure 3 suggests that the same grain boundary structure optimised for hardness also maximises the coating's resistance to interfacial delamination under Hertzian contact.

Table 2. Tribological Test Results at Selected Temperatures for 6% Al_2O_3 Nano-composite vs Reference Coatings

Material	Temp. (°C)	COF (steady state)	Wear Rate (×10⁻⁶ mm³/Nm)	Wear Mechanism
Uncoated HSS	25	0.62±0.04	18.4±1.2	Adhesive + Oxidative
Uncoated HSS	300	0.74±0.06	31.6±2.1	Adhesive + Oxidative
TiAlN (ref)	25	0.38±0.03	5.6±0.4	Abrasive (mild)
TiAlN (ref)	500	0.65±0.05	8.9±0.6	Oxidative + Abrasive
6% Al_2O_3 nano	25	0.31±0.02	2.9±0.3	Micro-ploughing
6% Al_2O_3 nano	300	0.33±0.02	3.4±0.3	Micro-ploughing + Glaze
6% Al_2O_3 nano	500	0.46±0.03	4.8±0.4	Glaze + Mild abrasive

4. Discussion

The finding that maximum hardness and tribological performance are achieved at 6% Al_2O_3 — rather than at higher Al_2O_3 contents that might intuitively be expected to maximise oxide coverage and oxidation resistance — reflects the fundamental

nano-composite design principle articulated by Veprek (1999): maximum strengthening in nc-MeN/a-binder systems requires a percolation-threshold grain boundary coverage below which the constraining stress exerted by the amorphous phase on the crystalline grains is maximised. Excess amorphous phase above the percolation threshold reduces constraining stress and introduces deformable intergranular regions that reduce bulk hardness and facilitate sub-surface cracking under tribological contact. The grain size of 8.2 nm measured for the 6% Al_2O_3 coating places it squarely in the reported optimal range for nano-composite hard coatings (5–15 nm), where the Hall–Petch hardening contribution from grain boundary strengthening is maximised without transition to the inverse Hall–Petch softening regime observed below approximately 5 nm grain size.

The superior elevated-temperature tribological performance of the nano-composite relative to reference TiAlN reflects both its structural thermal stability (retention of f.c.c. phase to 500°C versus 450°C for TiAlN) and the formation of a protective Al_2O_3 glaze layer that is kinetically facilitated by the pre-existing amorphous Al_2O_3 at grain boundaries. This in-situ oxide formation mechanism, analogous to the selective oxidation of aluminium-enriched coatings observed in TiAlN systems, provides a self-lubricating effect that partially compensates for the higher friction coefficients that would otherwise result from increased adhesive contact at elevated temperatures. The implications for cutting tool performance are significant: in dry face milling of AISI 4340 steel, the nano-composite-coated HSS end mills achieved an average tool life of 68 minutes compared to 20 minutes for uncoated HSS and 36 minutes for TiAlN-coated HSS — improvement factors of 3.4× and 1.9× respectively — which translates directly to reduced tooling cost per component in high-volume production.

The relatively modest improvement factor (1.9×) over TiAlN in tool life testing compared to the more dramatic wear rate improvement (52%) observed in laboratory ball-on-disc testing is attributed to the more complex multi-mechanism wear environment of the actual machining process, where edge chipping and notch wear at depth-of-cut boundaries — not captured by the ball-on-disc geometry — contribute to tool life termination criteria. The practical recommendation arising from this comparison is that the nano-composite coating provides the greatest performance benefit in continuous cutting operations at moderate feed rates and cutting speeds (250–350 m/min for hardened steels), where adhesive and oxidative wear at the rake face — the dominant mechanisms captured by the tribological testing protocol — control tool life.

5. Conclusion

This systematic study of TiAlN/Al_2O_3 nano-composite coatings deposited by magnetron sputtering on AISI M2 HSS substrates demonstrates that optimal Al_2O_3 incorporation at 6 vol.% produces coatings with significantly enhanced mechanical and tribological performance relative to both uncoated HSS and reference single-layer TiAlN. The principal findings are:

(i) The 6% Al_2O_3 nano-composite achieves hardness of 34.8 GPa and H^3/E_r^2 of 0.362 GPa, corresponding to 57% and 226% improvements respectively over the reference TiAlN coating, through a nano-composite strengthening mechanism involving grain boundary pinning by amorphous Al_2O_3 and associated Hall–Petch grain boundary hardening at the optimal crystallite size of 8.2 nm.

(ii) The nano-composite coating reduces wear rate by 84% relative to uncoated HSS and 48% relative to TiAlN at 25°C, with the wear rate advantage maintained at elevated temperatures to 500°C through the combined effects of superior structural thermal stability and in-situ Al_2O_3 glaze formation.

(iii) The correlation between H^3/E_r^2, adhesion strength, and tribological wear resistance across the Al_2O_3 composition range confirms that the 6% Al_2O_3 composition lies at the optimal grain boundary coverage for nano-composite strengthening and validates the H^3/E_r^2 parameter as a design criterion for predicting tribological performance from nanoindentation data alone.

(iv) Tool life improvement factors of 3.4× over uncoated HSS in face milling of AISI 4340 steel confirm the industrial significance of the nano-composite coating and suggest its suitability for deployment in medium-technology HSS tooling applications in the Indian manufacturing sector where lubricated and near-dry cutting conditions prevail.

Future work should investigate the fatigue behaviour of the nano-composite coating under interrupted cutting conditions, characterise the depth-dependent composition profile by XPS and TEM, and evaluate performance across a range of workpiece materials including titanium alloys and austenitic stainless steels where adhesive wear and built-up edge formation represent additional degradation challenges.

References

[1] Barshilia, H. C., Yogesh, K., & Rajam, K. S. (2009). Deposition of TiAlN coatings using reactive DC magnetron sputtering: Effect of Ar + N2 partial pressures. Vacuum, 83(2), 427-434.

[2] Bull, S. J., & Bhat, D. G. (2003). The indentation hardness of thin films. Journal of Physics D: Applied Physics, 36(12), R186-R197.

[3] Cheng, Y. H., Browne, T., Heckerman, B., & Meletis, E. I. (2010). Mechanical and tribological properties of nanocomposite TiSiN coatings. Surface and Coatings Technology, 204(14), 2123-2129.

[4] Derflinger, V., Brandle, H., & Zimmermann, H. (1999). New hard/lubricant coating for dry machining. Surface and Coatings Technology, 113(3), 286-292.

[5] Gupta, M., & Singh, K. (2021). Tribological characterisation of PVD-coated HSS tools in dry milling. Journal of Manufacturing Processes, 62, 14-26.

[6] Leyland, A., & Matthews, A. (2000). On the significance of the H/E ratio in wear control. Wear, 246(1-2), 1-11.

[7] Mayrhofer, P. H., Mitterer, C., Hultman, L., & Clemens, H. (2006). Microstructural design of hard coatings. Progress in Materials Science, 51(8), 1032-1114.

[8] Mohanty, S., Kumar, D., & Bhatnagar, N. (2019). Effect of PVD coating on HSS tool performance during machining of AISI D2 steel. Materials and Manufacturing Processes, 34(7), 756-768.

[9] PalDey, S., & Deevi, S. C. (2003). Single layer and multilayer wear resistant coatings of TiAlN: a review. Materials Science and Engineering A, 342(1-2), 58-79.

[10] Pvlicevic, J., Kisic, M., Vilotic, M., & Skoric, B. (2020). Nano-composite TiAlN/Al2O3 coatings for high-temperature tribological applications. Tribology International, 147, 106234.

[11] Sharma, A., Tiwari, S., & Dixit, A. R. (2016). Effects of minimum quantity lubrication (MQL) in machining processes. Materials Today: Proceedings, 3(6), 1960-1970.

[12] Singh, R., Pandey, A. K., & Mishra, R. (2020). Characterisation of TiAlN/Al2O3 coatings by nanoindentation and XRD. Thin Solid Films, 706, 138073.

[13] Veprek, S. (1999). The search for novel, superhard materials. Journal of Vacuum Science and Technology A, 17(5), 2401-2420.

[14] Veprek, S., & Reiprich, S. (1995). A concept for the design of novel superhard coatings. Thin Solid Films, 268(1-2), 64-71.

[15] Zhang, S., Sun, D., Fu, Y., & Du, H. (2003). Recent advances of superhard nanocomposite coatings: a review. Surface and Coatings Technology, 167(2-3), 113-119.